https://doi.org/10.1016/j.nanoen.2020.104484

Anion charge density disturbance induces in-plane instabilities within 2D lateral heterojunction of TMD: an atomic view

Mingzi Sun, Tong Wu and Bolong Huang*

Department of Applied Biology and Chemical Technology, The Hong Kong Polytechnic University, Hung Hom, Kowloon, Hong Kong SAR, China

*Email: bhuang@polyu.edu.hk

Abstract:

Two-dimensional (2D) transition-metal dichalcogenides (TMD) heterostructure semiconductors are emerging as the potential candidates for broad applications due to their flexible modulations of the electronic behaviors. However, the investigations of these TMD heterostructure semiconductors usually only limit to the synthesis approach and opt-electronic properties, lacking the in-depth guidelines from the atomic exploration of the formation and control of the disorder. Beyond the conventional disorder induced by the local fluctuations of inherent material properties such as chemical and structural composition, the fundamental concept of long-range phonon-based disorder has been identified in the single-layered TMD homogeneous structure [***Nat. Nanotechnol.*** 14, 832 (2019).]. Herein, we propose the essential long-range p-p coupling effecr in the more complex WSe_2/WS_2 lateral heterojunction systems, which leads to the formation of ripple in the macroscopic structure. The unique lattice dyanamic near the interface edge initiates the long-range disorder from the atomic view. Such long-range p-p couplings are confirmed by the large scale simulations by Forcite and the actual experimental scale simulations by COMSOL, supporting their pivotal role in modulating the electronic behaviors. This work has compensated the knowledge gap between the theoretical investigation and experimental synthesis, which is essentially beneficial for the future fabrication of 2D heterostructure semiconductors with superior performance.

Keywords: lateral heterojunction; p-p coupling; perturbation elastic entropy; density functional theory; transition-metal dichalcogenides

Introduction

Recently, the developments of the two-dimensional (2D) semiconductors are on full swing due to the legacy of the graphene success [1-2]. Besides graphene, the transition-metal dichalcogenides (TMDs) are emerging as the most potential 2D semiconductor systems, which have attracted tremendous interest due to the advantages of low-cost, earth-abundant, non-toxic, and environmentally friendly [3-8]. Owing to the atomically thin structure, unique electronic and optical properties and rich diversity in chemical compositions, they have displayed considerable potential in the applications of integrated optoelectronic devices and systems such as p–n diodes, photodetectors, transistors, nanogenerators, and sensors as well as in catalysis [9-17]. For example, Wang and his team have demonstrated the flexible and strain tunable MoS_2 based ultrathin heterojunction photodetector by the piezo-phototronic effect [14-15]. Owing to superior stability, the appropriate direct bandgap, and moderate mobility, the atomically thin MoS_2 also shows impressive progress in the field-effect transistor (FET) and triboelectric nanogenerators (TENG) [13, 16-17]. Most importantly, the distinguishable piezoelectric performance between the odd number and even number of MoS_2 layers are confirmed through experiments by Wang's group [3]. These works indicate the great potential of 2D TMD materials by coupling between piezoelectricity and semiconducting properties. Until now, diverse 2D heterostructure semiconductors have been intensely studied in experiments regarding the synthesis approach and unique electronic structures. Such materials possess spatially tunable bandgap alignments and sharp interfaces, which are of pivotal significance and opens the opportunities in the high-performance device applications [18-20]. In particular, the growth of such structures has achieved impressive progress from the mechanical stacking approach to direct growth strategy. For example, Wang *et al.* have synthesized the few-layer stacked WSe_2/SnS_2 device through a mechanically exfoliated and restacked method [21]. Zhang et al. demonstrated the stacking growth of few layers of WSe_2 on the randomly oriented SnS_2 [22].

Compared to the more facial synthesis of vertical TMD heterostructures [23-25], the lateral growth is considered as a challenge due to the demands for advanced growth protocols. With the devoted attention and investigations, the appearance of edge epitaxial strategy has solved this challenge and accelerates the developments of lateral heterojunction structures. For example, Li and co-workers demonstrated a two-step epitaxial growth of the atomic thick lateral WSe_2/MoS_2 heterojunction [26]. In their work, the edge of WSe_2 induces the epitaxial MoS_2 growth even they show a large lattice mismatch. Later, they further developed a new process for achieving large-scale high-quality WSe_2/MoS_2 lateral heterojunction interfaces [27]. The growth of such lateral junctions allows novel functional devices, such as in-plane transistors and diodes, to be integrated within a single atomically thin layer. Duan *et al.* have reported the lateral growth of $MoS_2/MoSe_2$ and WS_2/WSe_2 heterostructures to actualize the atomic p–n diodes [28]. Moreover, Gong et al. have proved the synthesis of the lateral WS_2/MoS_2 heterostructures also correspondingly modifies the optical emission of the in-plane direction [24]. Thus, the optoelectronic properties of the fabricated semiconductor heterostructures directly correlate to their energy band diagram at their interfaces. Since the observed unique properties of heterostructure predominantly stem from the junction, the goal of obtaining a high-quality junction is driving the innovations in the present research.

Within the lateral heterojunction, the unique ripple effect has been identified as the consequence of the important interplay between different TMDs (**Figure 1**). Through the atomic force microscopy (AFM) within $MoS_2/MoTe_2$, which is ascribed to the lateral gradients in Te substitution levels and coupling effect between 2H and 1T phases [29]. The coherence between different TMDs is also confirmed by Park *et al.* [30]. Through the precise control of such ripple geometry, Rogers and coworkers confirm the high performance of such unique heterojunction stretchability, compressibility and bendability [31]. Although experimental works have achieved significant results, the in-depth theoretical investigations of such unique structure features are still very limited. Usually, the first principle calculations are applied to study the electronic properties and band alignment. Dai *et al.* revealed the strain in different TMD combination, which induced the bandgap variation [32]. Similarly, Sun *et al.* also reflected the geometric and electronic properties of the interface within the TMD lateral heterostructures by the first principle calculations [33]. Another work by Yang *et al.* also applied density functional theory (DFT) to discuss the photoexcitation charge transfer and energy transfer dynamics of lateral MoS_2/WSe_2 heterojunctions [34]. Recently, Jiang utilizes the LAMMPS package to reproduce the misfit strain-induced buckling in the MoS_2/WSe_2 with molecular dynamics (MD) simulations [35]. The in-depth understanding of the general explanation of the lateral heterojunction structures still requires the integration of theoretical guidance and experimental design to actualize the future fabrication of 2D lateral heterostructure semiconductor systems. Thus, in this work, we have proposed the guidelines to identify the charge disturbance induced by the anion coupling effect to explain the formation of the ripple structure within the 2D WSe_2-WS_2 lateral heterostructure. This work supplies the fundamentally general mechanism for the experimentally observed phenomenon, which is of pivotal significance in the further exploration in such 2D heterojunction semiconductor materials.

Results and Discussion

Beyond the static lattice model, the lattice dynamics extends the concept of the crystal lattice to a collective vibration of atoms, which reflects both inter-ionic and electronic density fluctuations in affecting the lattice vibrations. To illustrate the origin of the ripple effect in the lateral heterojunction structures, we firstly demonstrate the phono dispersion of the typical single-layered TMDs for comparison including MoS_2, WS_2 and WSe_2 (**Figure 2A-2C**). Notably, the acoustic branches of these three typical TMDs are gradually decreasing from 230 cm^{-1} in MoS_2 to 140 cm^{-1} in WSe_2. Meanwhile, the shrink of the optical branch is slighter, which reduces from 180 cm^{-1} in MoS_2 to 130 cm^{-1} in WSe_2. Especially, the change of the cation atoms shows a much smaller influence on the optical branches than the anion atoms, indicating the crucial effect of the anion in affecting the lattice vibration. Then, the phonon dispersions of the WS_2-WSe_2 lateral structures are considered in different interfacial ratios. For the WS_2-WSe_2 lateral structure with 1:1 ratio, the interfacial structure shows high stability due to the absence of the imaginary frequency (**Figure 2D**). The instability induced by the interactions between the S-Se is counteracted within a small region. When the wavevector $\boldsymbol{q}$ is larger than 0.4, we notice the evident disturbance on the phono dispersion with an oscillating effect even near the high-symmetry gamma point. Such disturbance on the phonon dispersion becomes more evident with the imaginary frequency at a higher ratio (**Figure 2E**). This represents that the strong charge inhomogeneity induced by the interactions between S-Se further leads to structural instability. Compare to WS_2/WSe_2 lateral structure with 2:2 ratio, the lateral structure with 3:1 ratio shows even stronger entanglement of optical branches, which is ascribed to the more inhomogeneous charge distribution (**Figure 2F**). The Brillouin zone of the lateral heterojunction structures with the different ration between WS_2 and WSe_2 displayed in **Figure 2G-2I** with a similar electron transfer pathway. Especially for the thin film with fluctuations, the induced anion couplings cause the charge disturbance, which inevitably leads to the anomalies electronic behaviors with energy transfer, leading to the ripple structure in the atomic thin 2D materials [36-37]. The phonon dispersion based on the periodic unit cells demonstrates the evident electronic fluctuations near the edge, which supports the further extension of the coupling effect to the long-range level. Based on the phonon dispersion, we deduce that the evident inhomogeneous charge distribution in the atomic interfacial region is dominated by the S-Se coupling effect, which requires further verification in the lateral heterojunction structures.

Inspired by the previous experiment synthesis [38-39], we construct the single-layer WSe_2-WS_2 lateral heterojunction based on the triangle WSe_2 within WS_2 to investigate their formation process. We started from the isolated WS_2/WSe_2 lateral heterojunction that includes a mono WSe_2 triangle with 30.37 Å edge length. Notably, the peripheral area outside the WSe_2 has exhibited a roughly snowflake-like pattern, which is distinct from the original structure of WSe_2 and WS_2 (**Figure 3A**). The surface vibration has induced the newly formed superstructure that possesses a different symmetry and periodicity. From the enlarged display of the WSe_2 core, the good periodicity of the new superstructure originated from the central WSe_2 is observed (**Figure 3B**). The structural evolution from the original P63/mmc hexagonal crystal structure is mainly achieved by the rotation of S and Se sites to form the octahedral unit with stable W sites, supporting the lack of short-range disorder (**Figure 3C**). To further confirm the influence of the array arrangement to the appearance of the superstructure, we compare the horizontal triangle array with the vertical triangle array. Compare to the original structure, the existence of the superstructure is confirmed in the horizontal triangle array (**Figure 3D- 3E**). The size of the superstructure shrinks compared with that in the mono WSe_2 triangle. Between two WSe_2 triangles, the connected region has shown the widest length of the superstructure of 28.22 Å, with the longest length in the vertical direction of 22.50 Å, which are 3.1 times and 2.5 times of the space between two triangles, respectively. On the contrary, the vertical array exhibits a slightly smaller influence on the formation of the superstructure (**Figure 3F**). The results of different array arrangements confirmed that the existence of the superstructure is not induced by the quantum effect that depends on the size, which is the unique feature result from the competition between local Se and S atoms. Thus, the anomaly singularity electron-rich in the heterojunction area massively reduces the lattice stability driven by the electron-lattice coupling effect that follows the Mott-Anderson transition model [40] (**Figure 3G**). To recover to the stable lattice, the whole structure undergoes the relaxation to deplete the intrinsic instability. Thus, the structure relaxation leads to the distorted lateral heterojunction structure.

Besides the understanding of lattice distortion, the quantitative energetic analysis regarding the variation of valence energy and van der Waals (vdW) energy in the strain-induced superstructure. As the array number increases, the strong surface valence and vdW fluctuation result in the instability of the structure accompany with the dramatic energy increase to the energy window (**Figure 3H**). The competition between the superstructure and the original structure reaches a balance during the energy window, explaining the similar energy trend within this period. As the array keeps increasing, the superstructure becomes dominant that significantly stabilizes the structure to lower the overall energy. The size change of the superstructure shows a downhill trend that illustrates the offset effect between the superstructures (**Figure 3I**). The size of the superstructure region shows less change during the energy window, which is consistent with an offset between superstructures. The dominating role of the superstructure is also verified after a specific increase in the arrays. As another important factor to determine the stability of 2D heterojunction, the mechanical properties of these arrays are also investigated (**Figure 3J**). Similar fluctuations noted on both the Poisson's ratio and shear modulus, especially at the intermedium states with strong strain effect induced by the superstructure, supporting the in-plane instability induced by the anion coupling. As the array number keeps increases, the instability effect is counteracted by the array coupling, which significantly minimizes the strain effect and achieves an optimally negative Poisson's ratio, enhancing their mechanical properties for diverse applications. The shear modulus is also stabilized to a low level with a good ductility rather than high rigidity, which supports the alleviation of the in-plane instability induced by anion coupling effect. More interestingly, the array correlation effect induced by the space arrangement is also discussed in detail. In the horizontal space, as the space width between the triangle keeps increasing, the overall energy experiences an evident drop within a limited region, indicating the coupling effect between the arrays affects the structure in a small range (**Figure 3K**). Such an effect is size-dependent, which is essential for small-scale samples while disappearing in large space arrangements. In comparison with the horizontal array arrangements, the vertical arrays imposed a subtle coupling effect between the arrays (**Figure 3L**). As space becomes larger, the superstructures become isolated, which shows little correlation with other arrays, which is confirmed by the continuous downhill trend of both valence energy and vdW energy. The size-effect of the triangle is also considered as shown in **Figure 3M**. To alleviate the induced strain, the internal and peripheral distortion becomes more evident as the size increases that aggravate the instability of the lattice with increased energy. Surprisingly, the nearly linear fitting between the triangle size and the energy is depending on the logarithmic relationship rather than the triangle area size, demonstrating a low surface energy correlation to the formation of the superstructure. With these preliminary results, the inevitable superstructure formation has been verified for the WSe_2-WS_2 lateral heterojunction array due to the intrinsic strain effect. The structure distortion results from the coupling effect between arrays, indicating the space arrangement rather than the quantum effect.

Based on the CASTEP calculations, the electronic structure has been considered to investigate the intrinsic interplay between WS_2/WSe_2 lateral heterojunction interface. From the projected partial density of states (PDOS) shows the p-orbitals of the S-Se near the interface edge, we notice the abnormal occupied states crossing the Fermi level (E_F), which shows a range of 0.25 eV to 0.30 eV in different scale of the lateral heterojunction systems (**Figure 4A**). The energy range represents the tailor state coverage ranges, which is strongly correlated with the p-p coupling effect on the formation of the superstructure and the ripple. The appearance of the tail states at the edge of the valence band indicates the long-range disorder with the loss of the van-Hove singularity. Such a unique coupling state is ascribed to the long-range p-p coupling effect between S and Se atoms, which largely enhances the electron agglomeration near the heterojunction surface. This further causes the energy releasement in pulse mode to initiate the rippled structure driven by negative correlation energy [41-42]. The 3D orbital distribution of the single-layer heterojunction supports the evident electronic overlap between Se and S atoms. The electronic inhomogeneity further induces the ripple structure. Due to the orbital coupling between the non-bonding long pairs in S and Se atoms, the strong p-p coupling leads to the lone pair saturation for higher orbital stability, accompanied by the local structural change (**Figure 4B**). The thermodynamic formation enthalpy difference between WSe_2-WS_2 is another dominant reason for the long-range disorder of the superstructure. To understand the origins of the superstructure, we have we derive the perturbation elastic entropy in the lattice as Eq. (1) to correlate the energy and local superstructure size. The derivation can be found in supporting information [43].

$$E = ST = \frac{qQN_A}{8\varepsilon_s} x^2 \quad (1)$$

The q is the electronic charge induced by strain effect. The Q represents the perturbation charge, which is approximate 0.1 scale of q in each WSe_2-WS_2 unit. The ε_s is the dielectric constant of the WSe_2 and N_A is the Avogadro number. The ripple size is generated by the valence p-π tail states, which is derived to ~0.1 μm scale. Based on the evident formation enthalpy (~30 eV) difference between WSe_2 and WS_2 individual units, the length of the superstructure is also deduced to the micrometer scale. The anomaly singularity electron-rich in the heterojunction area massively reduces the lattice stability driven by the electron-lattice coupling effect that follows the Mott-Anderson transition model [40]. For the simulation of sub-micrometer, we have introduced the Forcite method to observe the structure change and corresponding mechanical properties variations. To recover to the stable lattice, the whole structure undergoes the relaxation to deplete the intrinsic instability through the formation of ripple, which suffers the largest strain (**Figure 4C**). The enlarged details of the p-p coupling are clearly found in the heterojunction boundary and the apex area of WSe_2. The left figure in **Figure 4D** represents the superstructure at the edge of the WSe2 while the right figure indicates the superstructure near the apex of WSe_2. The long-range p-p coupling strength is weakened as the distance increases that lead to the observation of the transition area from the original WS_2 structure to the superstructure. The superstructure is also formed inside the WS_2 as the origins of the strain (**Figure 4E**).

Beyond the lattice structure and theoretical derivation of the ripple phenomenon, the p-p coupling effect towards array is also analyzed from the energetic perspective and mechanical properties. It is found that the mechanical property of Poisson's ratio is gradually stabilized from the strong fluctuation as the system energy decreases to a stable level (**Figure 4F**). The strain of the system is released as the formation of the superstructure, lowering the instability of the heterojunction structure (**Figure 4G**). More importantly, we consider the influence of the array distances on the stability of the heterojunction system by the formation of the superstructure. For the transverse direction, the lattice experiences an energy minimum when the superstructure formation ratio is the largest, supporting the strain releasement by the superstructure.

For the longitudinal direction, the strain simply decreases with the distances between the array and achieves a stable period (**Figure 4H**).

After the detailed analysis between the interaction of two arrays, the further expansion of the array scales is required to reveal the actual synthesis conditions. By considering the array up to 3×3, we further map the strain in the WSe_2-WS_2 lateral heterojunction with different number arrays. Firstly, we measure the size of the ripple of different scale WS_2/WSe_2 lateral heterojunction interface. Notably, the height of the ripple is also quantified by the sampling of different period lengths near the WS_2/WSe_2 interface. Notably, the heights of the ripples are relatively even, which is distributed around 0.8 nm to 1 nm. Thus, the theoretical simulations of the ripple structure parameters show good consistency with our theoretical derivation based on the concept of perturbation elastic entropy (**Figure 5A**). Then, the density of the strain is demonstrated. As the size increases, the strain becomes more selectively distributed, which is gradually concentrated on the WSe_2/WS_2 interface (**Figure 5B**). Meantime, the WSe_2 and WS_2 are experiencing the tensile strain. The strong array couplings near the apex are noted when the arrays are aligned in the transverse direction, which leads to the highly compress strain. In comparison, the internal area of WSe_2 and neighboring WS_2 show the evident tensile strain. When the array start aligns in the longitudinal directions, some other strain appears that counteract the concentrated strain near the apex while the strain inside WSe_2 remains tensile (**Figure 5C**). As the number of arrays keeps increasing, the strain becomes more evenly distributed and the tensile strain contrast becomes weaker between WSe_2 and WS_2. More importantly, the strain agglomeration is noted near the WS_2/WSe_2 interface. In addition, we perform the large-scale dynamic simulation to observe the formation evolution of the ripple between WSe_2 and WS_2. To reproduce the synthesis process, we start the initial simulation of 1 μm scale of the WSe_2 triangle. It is noted that the induced strain between WSe_2-WS_2 has caused an evident distortion with the large area of the superstructure formation near the interface area between WSe_2 and WS_2 (**Figure 5D)**. The formed ripples mainly centralize in WS_2 region showing irregular growth orientations. As the size of WSe_2 increasing to around 2 μm scale, we observe more evident misaligned local ripples with a distinct height difference in the z-axis (**Figure 5E)**. The ripple direction in WSe_2 displays around 45 °angle close to the diffusing configuration near the apex of WSe_2 arrays. Notably, as the size of the WSe_2 triangle increases to 4 μm, the ripple becomes parallel extending from internal WSe_2 towards WS_2(**Figure 5F)**. The width of each band is around 0.15 μm, supporting our previous theoretical predictions. The further increases of the WSe_2 arrays result in more patterned configurations, where the ripples are closer with a slightly smaller width (**Figure 5G)**. The ripple becomes blurred at the middle of the triangle edge in the WSe_2 arrays, indicating the limited affecting range of the p-p couplings. In comparison with the previous work without the consideration of the long-range interactions, we have further confirmed the ripple structure induced by the out-of-plane strain. Such a ripple formation is induced by the dynamic strain during the thin film growth by the CVD method, which is very difficult for DFT to monitor the transient interactions. However, the static instability and strain simulation have been well consistent with the previous work [35].

The thermodynamic calculations based on the quench condition of the typical CVD experimental approach (900-1100 K) all show a positive correlation between the strain and the lattice stability. After the quenching procedure, an evident tensile strain is noted on the single-layer WS_2/WSe_2 lateral heterojunction based on the lattice constant change. For an individual WSe_2 triangle growth, both strain and normalized energy of WSe_2 display a similar fluctuation as the size of WSe_2 increases, indicating the complicated entanglement between thermal expansion and WS_2/WSe_2 interaction (**Figure 5H**). However, such random strain change becomes regulated as the array scale increase. Notably, the tensile strain is finally reduced to around 3.5% when arrays form scale (**Figure 5I**). The high concentration of WSe_2 facilitates the strain releasement by the interaction between arrays in a well-regulated growth pattern. Following the strain releasement, the energy also keeps decreasing to a stable level. In addition, as the array distance between WSe_2 is enlarged, the tensile strain undergoes a sudden drop and then stabilizes near 5%, which demonstrates the disappearance of the array interaction (**Figure 5J**). The comparison between the pristine WS_2 and WS_2 with growth pores confirms the assistance of the pores in WS_2 to the thermal expansion at high temperatures (**Figure 5K**).

Compared to the actual experiments, our previous simulations are still much smaller than the typical experimental synthesis scale. To verify the ripple structure in the real experimental fabrication of lateral heterojunction, the COMSOL simulation is utilized to reproduce the corresponding strain distribution within the lateral heterojunction. All the models have been built close to the actual experimental size, in which the edge of WSe_2 triangle is 10 μm while the WS_2 substrate shows an edge of 50 μm. The simulation results at room temperature (298 K) demonstrate the whole material is under tensile strain even after cooling from 1173 K. Notably, the formation of ripples shows similar results with the theoretical predictions **(Figure 6A)**. In both horizontal and vertical directions, we notice the ripple region surrounded the WSe_2 triangles, which is highly similar to the observation of superstructure in DFT calculations (**Figure 6B and 6C**). By increasing the deformation scaling parameters, the strong compress strain is noted on the edges of WSe_2 triangles, supporting the theoretical predictions and previous experiments (**Figure 6D**) [44]. More importantly, slight ripples structures are also noted inside the triangles domains, which is consistent with DFT calculations. The strongest tensile strain level is presented around the triangles on the plate while a weaker tensile strain is presented inside the triangle domains. This difference around the rims suggests the plate has compressed the triangles under the effect of heat (**Figure 6E**). The strongest tensile strain locates at the sharp apex of the triangles with the contact of the plate, while the other parts of the triangle preserve a lower level of tensile strain, supporting our microscopic strain distribution (**Figure 6F**). We further studied the influence of interval distance based on models of WSe_2-WS_2 with different spacing between the WSe_2 triangles. The spacings of 2 μm, 3.5 μm and 5 μm are investigated to the same deformation level to compare the distortion. Unexpectedly, the 2 μm spacing model shows the weakest tensile strain level (**Figure 6G**). By comparing the strain between 3.5 μm and 5 μm interval models, the 5 μm model reports the largest maximum strain value while the 3.5 μm model presents higher tensile strain in the “ripple” region. The compress effect on the triangle’s edges is obviously increasing as the spacing increases from 2 μm to 5 μm. This phenomenon is ascribed to that larger space between the triangles allows the plate to expand more freely, which in turn increases the pressure difference at the rim of the triangles and thus the plate squeezes the triangles harder (**Figure 6H and 6I**). Thermal expansion simulation of the WS_2 with pores for growth of WSe_2 is also demonstrated at the growth temperature of 900 °C, which further leads to the subsequent deformation on the premade triangle-pores. This phenomenon is noted in both 2D and 3D models. Due to the tensile strain from the substrate WS_2 expansion, the triangle pores are suppressed with inward deformation. The colormap shows the largest strain locates at the edges of the triangle-pores (**Figure S1**).

Conclusion

In summary, the anion coupling induced charge disturbance within the WSe_2-WS_2 lateral heterojunction has been identified as the origin of the ripple structure induced by in-plane interfacial instability. Different scales of the first-principle simulations all verify the similar ripple phenomenon near the interfacial region of the WSe_2-WS_2 lateral heterojunction. Beyond the simple factor of lattice misfit, we confirm that the Se-S p-p coupling effect induced the uneven charge distribution is the intrinsic reason for such a unique structural phenomenon. More importantly, we introduce the perturbation elastic entropy concept to predict the scale of such a ripple structure, which shows high consistency with the simulation results of experimental scale systems. For the bulk strain distribution, the tensile strain inside the bulk WSe_2 and WS_2 are noted while the interface region undertakes the compress strain. This work has supplied insightful references for the intrinsic properties for 2D lateral heterojunction structures. which not only demonstrates the unique ripple structure by different scale simulations but also indicates the in-depth theoretical understanding for the first time. This work is of significance for the future design of novel 2D heterojunction semiconductors.

Acknowledgements

The authors gratefully acknowledge the support of the Natural Science Foundation of China (Grant No.: NSFC 21771156), and the Early Career Scheme (ECS) fund (Grant No.: PolyU 253026/16P) from the Research Grant Council (RGC) in Hong Kong.

Declaration of interest

The authors declare no competing interest.

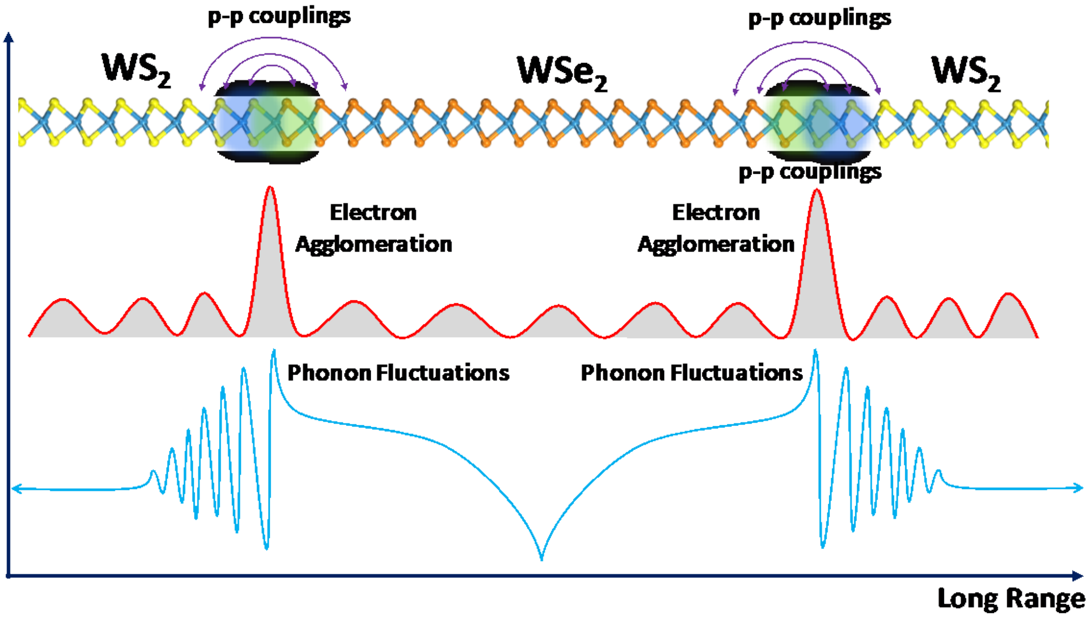

Figure 1. The illustration of p-p couplings phenomenon in the 2D lateral heterojunction.

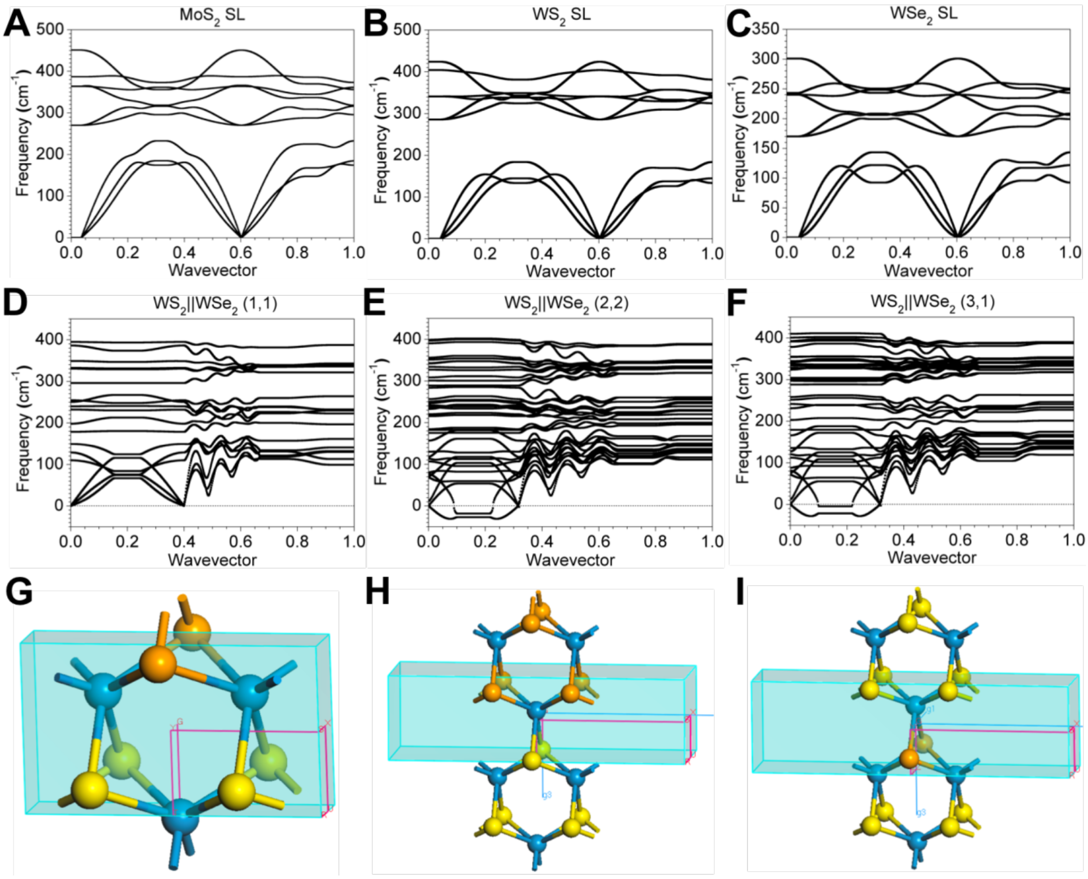

Figure 2. The phonon dispersion of single layer **A.** MoS_2, **B.** WS_2 and **C.** WSe_2. The phonon dispersion of WS_2-WSe_2 lateral interface with different ratio. **D.** WS_2: WSe_2 = 1:1; **E.** WS_2: WSe_2 = 2:2 and **F.** WS_2: WSe_2 = 3:1. The Brillouin zone of the lateral interface structure with different ratio. **G.** WS_2: WSe_2 = 1:1; **H.** WS_2: WSe_2 = 2:2 and **I.** WS_2: WSe_2 = 3:1. The orange balls = Se atoms; the yellow balls = S atoms and the blue atoms = W atoms.

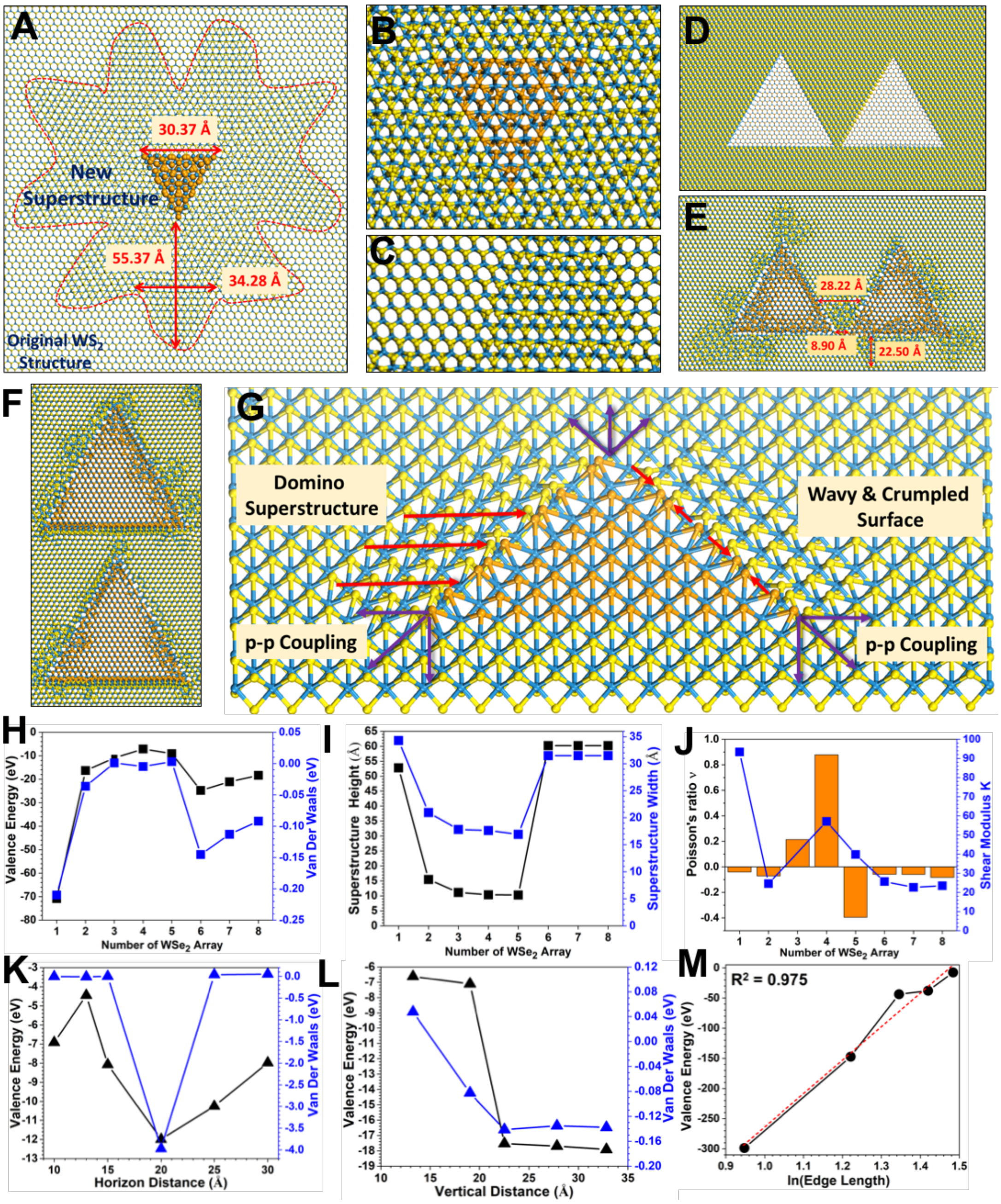

Figure 3. A. Illustration of the superstructure formed around the WSe$_2$ triangle. **B.** Relaxed structure of single WSe$_2$. **C.** Demonstration of the edge of superstructure. **D.** Original structure of double horizon WSe$_2$ triangle array and **E.** the relaxed structure. **F.** The relaxed structure of vertical WSe$_2$ triangle array. The **G.** The mechanism diagram of p-p coupling induced superstructure in WSe$_2$-WS$_2$ lateral heterojunction. Original structure of the horizontal WSe$_2$-WS$_2$ lateral heterojunction array. The dependence of the **H.** energy, **I.** superstructure size and **J.** mechanical properties on the number of WSe$_2$ arrays. **K.** The energy dependence on the horizontal space arrangement between arrays. **L.** The energy dependence on the vertical space arrangement between arrays. **M.** The energy dependence on the size of the WSe$_2$ triangle.

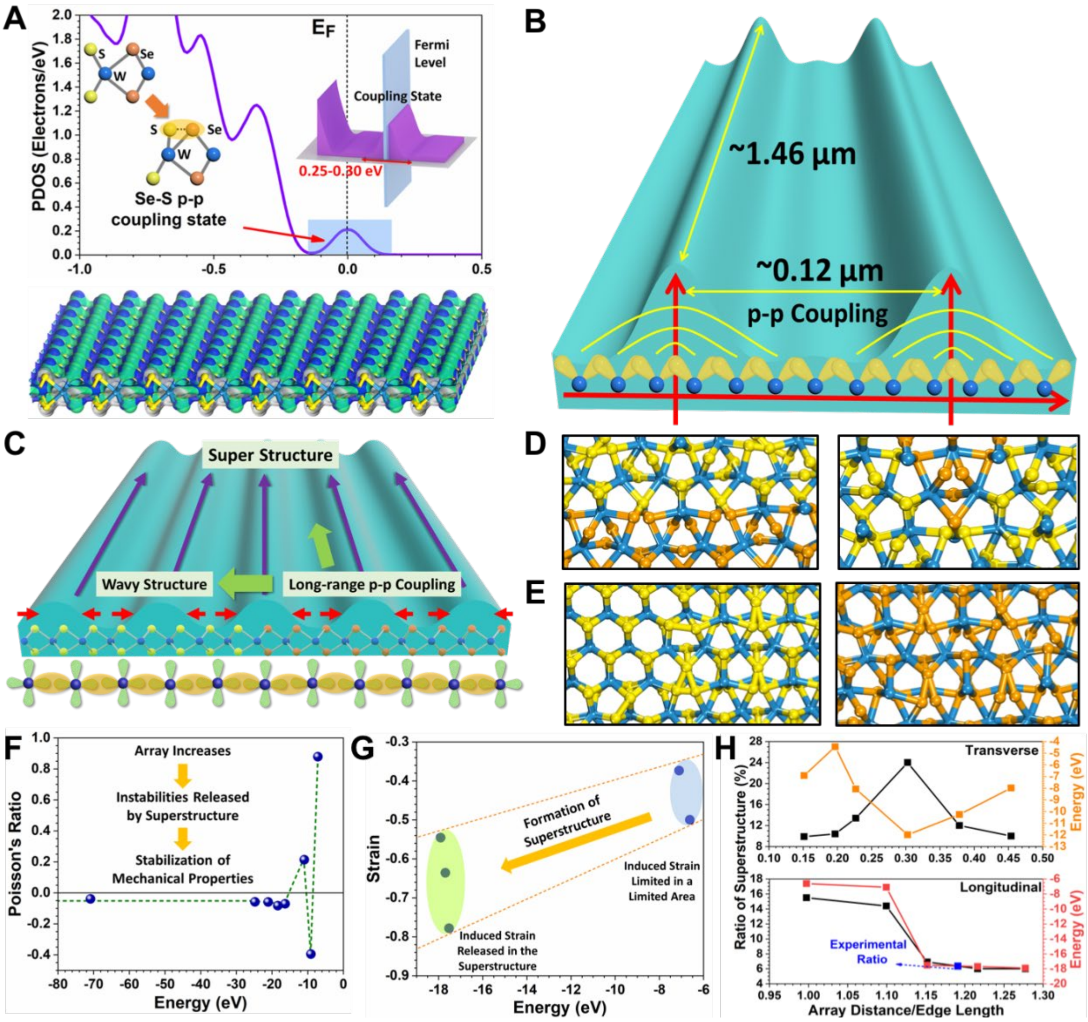

Figure 4. A. Coupling states by p-p coupling in PDOS of WSe_2-WS_2 lateral heterojunction systems and their 3D orbital distribution. **B.** Schematic illustration of the superstructure scale by the long-distance p-p coupling effect formed around the WSe_2 triangle. **C.** The mechanism diagram of p-p coupling induced superstructure in WSe_2-WS_2 lateral heterojunction. **D.** Enlarged display of the boundary and the apex area of heterojunction system. The left figure represents the superstructure at the edge of the WSe_2 while the right figure indicates the superstructure near the apex of WSe_2. **E.** Enlarged display of the transitional superstructure and the superstructure inside WSe_2. The left figure demonstrates the edge of the structure within the WS_2 and the right figure illustrates the superstructure inside the WSe_2. **F.** The correlation between the mechanical properties and the system energy. **G.** Dependence of strain change in the system energy. **H.** The energy change of the WSe_2 array scale and arrangement.

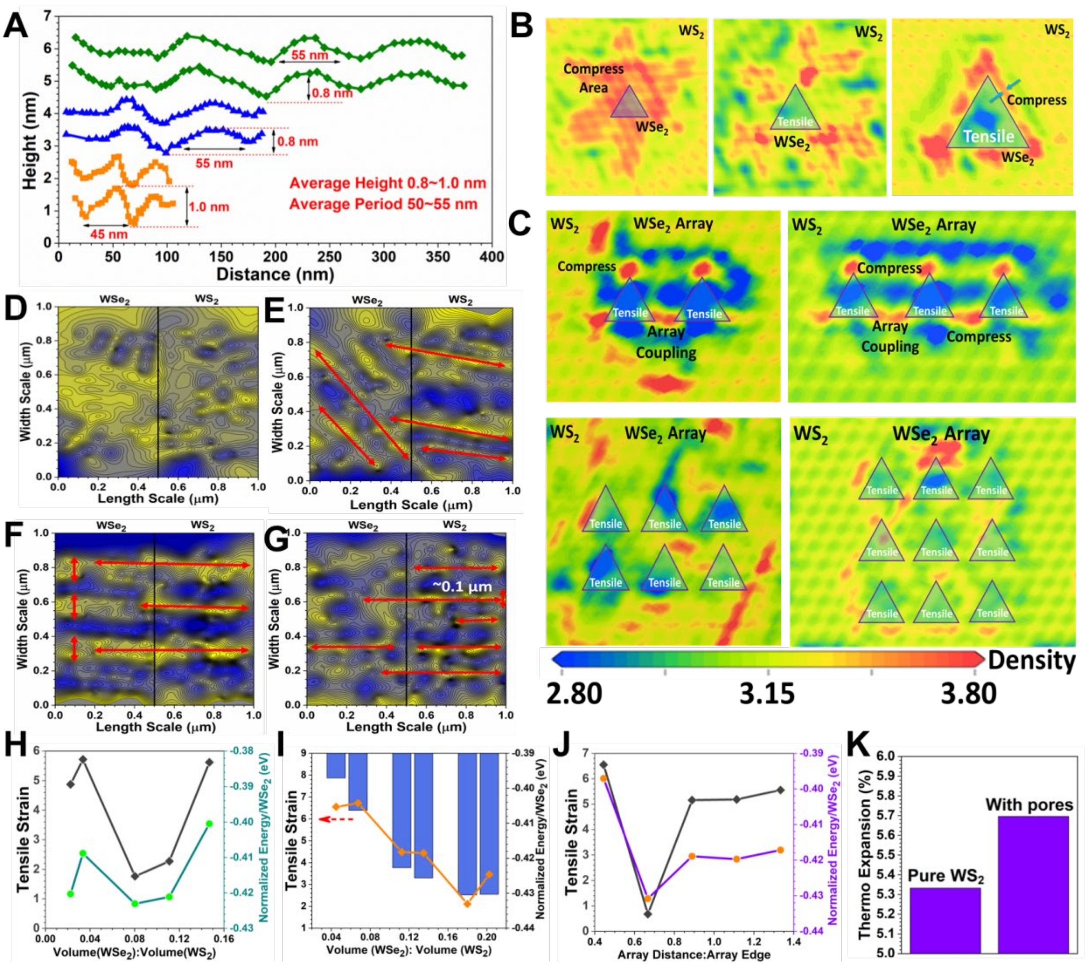

Figure 5. A. The sampling of ripple height in WSe$_2$-WS$_2$ lateral heterojunction systems. **B.** The dependence of density distribution with the WSe$_2$ size. **C.** The dependence of density distribution with the WSe$_2$ array arrangements. **D.** The initial surface distortion at 1 μm scale WSe$_2$ array. **E.** The diffusing ripple at 2 μm scale of WSe$_2$ array. **F.** The well-aligned ripple at 4 μm scale of WSe$_2$ array. **G.** The compact ripple at 8 μm scale of WSe$_2$ array. **H.** The dependence of strain with the individual WSe$_2$ size. **I.** The dependence of strain with the scale of WSe$_2$ arrays. **J.** The dependence of strain with the transverse distance between WSe$_2$ arrays. **K.** Thermal expansion comparison between pure WS$_2$ and WS$_2$ with growth pores.

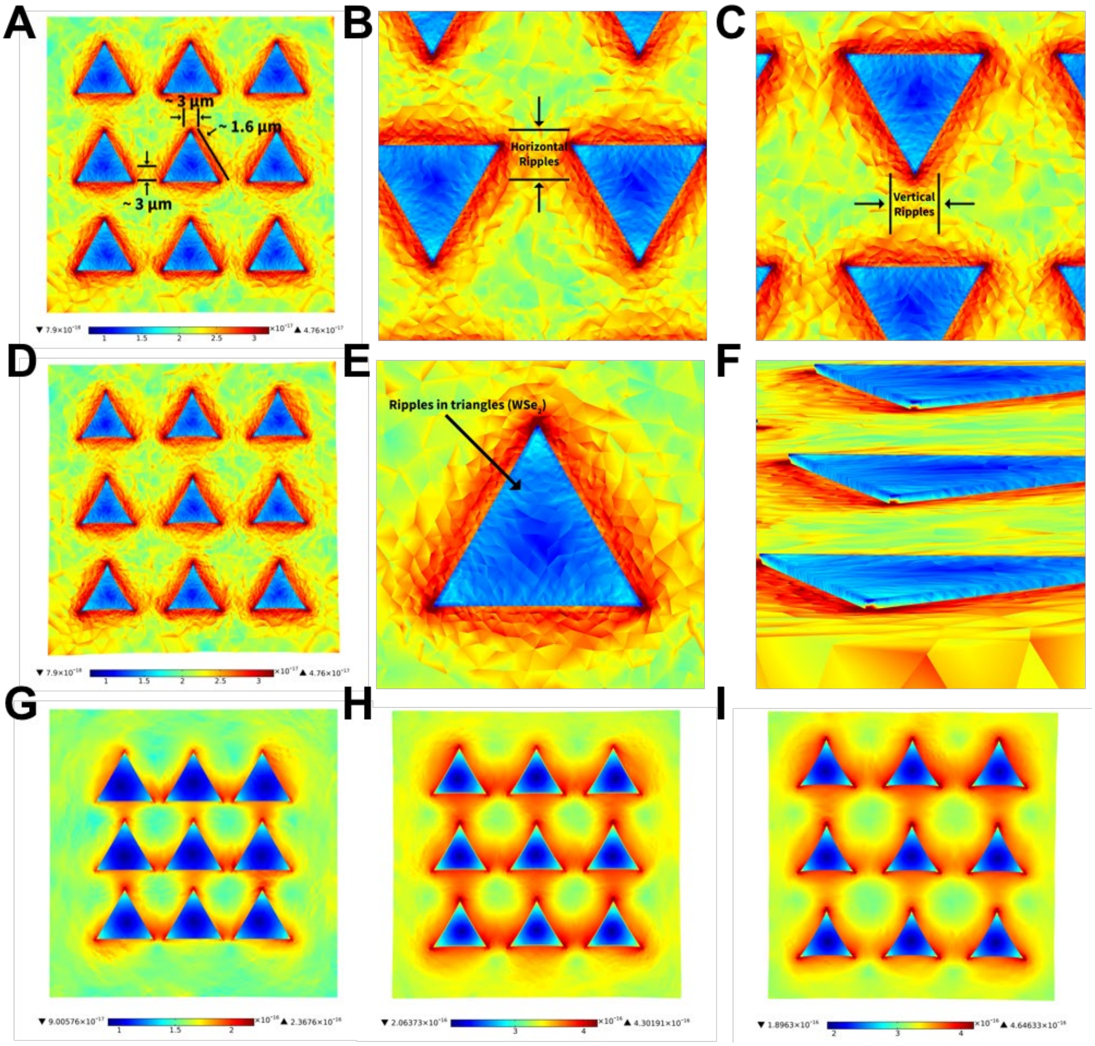

Figure 6. The first principal strain mapping on the WSe_2-WS_2 surface by COMSOL. **A.** The XY-plane view of the model. Observed ripple regions are marked and annotated with approximate distance. **B, C**. Horizontal and vertical ripples between the WSe_2 triangles. **D.** Deformation level is scaled up from 0.1 to 1 in COMSOL to observe the slight deformation of triangles. **E.** Ripples inside the triangle domains. **F**. Angled-view of the surface. The 2D models with varying spacing between triangles of **G**. 2 µm, **H**. 3.5 µm and **I.** 5 µm.

References

[1] D. Akinwande; C. Huyghebaert; C.-H. Wang; M. I. Serna; S. Goossens; L.-J. Li; H. S. P. Wong; F. H. L. Koppens, Graphene and Two-Dimensional Materials for Silicon Technology. *Nature* **2019,** *573* (7775), 507-518.

[2] Y. Qin; X. Wang; Z. L. Wang, Microfibre-Nanowire Hybrid Structure for Energy Scavenging. *Nature* **2008,** *451* (7180), 809-13.

[3] W. Wu; L. Wang; Y. Li; F. Zhang; L. Lin; S. Niu; D. Chenet; X. Zhang; Y. Hao; T. F. Heinz; J. Hone; Z. L. Wang, Piezoelectricity of Single-Atomic-Layer Mos2 for Energy Conversion and Piezotronics. *Nature* **2014,** *514* (7523), 470-4.

[4] M. Chhowalla; H. S. Shin; G. Eda; L.-J. Li; K. P. Loh; H. Zhang, The Chemistry of Two-Dimensional Layered Transition Metal Dichalcogenide Nanosheets. *Nature Chemistry* **2013,** *5* (4), 263-275.

[5] J. N. Coleman; M. Lotya; A. O'Neill; S. D. Bergin; P. J. King; U. Khan; K. Young; A. Gaucher; S. De; R. J. Smith; I. V. Shvets; S. K. Arora; G. Stanton; H. Y. Kim; K. Lee; G. T. Kim; G. S. Duesberg; T. Hallam; J. J. Boland; J. J. Wang; J. F. Donegan; J. C. Grunlan; G. Moriarty; A. Shmeliov; R. J. Nicholls; J. M. Perkins; E. M. Grieveson; K. Theuwissen; D. W. McComb; P. D. Nellist; V. Nicolosi, Two-Dimensional Nanosheets Produced by Liquid Exfoliation of Layered Materials. *Science* **2011,** *331* (6017), 568-571.

[6] X. Qian; J. Liu; L. Fu; J. Li, Quantum Spin Hall Effect in Two-Dimensional Transition Metal Dichalcogenides. *Science* **2014,** *346* (6215), 1344-1347.

[7] K. Tran; G. Moody; F. Wu; X. Lu; J. Choi; K. Kim; A. Rai; D. A. Sanchez; J. Quan; A. Singh; J. Embley; A. Zepeda; M. Campbell; T. Autry; T. Taniguchi; K. Watanabe; N. Lu; S. K. Banerjee; K. L. Silverman; S. Kim; E. Tutuc; L. Yang; A. H. MacDonald; X. Li, Evidence for Moiré Excitons in Van Der Waals Heterostructures. *Nature* **2019,** *567* (7746), 71-75.

[8] C. Huang; S. Wu; A. M. Sanchez; J. J. P. Peters; R. Beanland; J. S. Ross; P. Rivera; W. Yao; D. H. Cobden; X. Xu, Lateral Heterojunctions within Monolayer Mose2–Wse2 Semiconductors. *Nature Materials* **2014,** *13* (12), 1096-1101.

[9] Z. Lin; Y. Liu; U. Halim; M. Ding; Y. Liu; Y. Wang; C. Jia; P. Chen; X. Duan; C. Wang; F. Song; M. Li; C. Wan; Y. Huang; X. Duan, Solution-Processable 2d Semiconductors for High-Performance Large-Area Electronics. *Nature* **2018,** *562* (7726), 254-258.

[10] J. W. Chen; S. T. Lo; S. C. Ho; S. S. Wong; T. H. Vu; X. Q. Zhang; Y. D. Liu; Y. Y. Chiou; Y. X. Chen; J. C. Yang; Y. C. Chen; Y. H. Chu; Y. H. Lee; C. J. Chung; T. M. Chen; C. H. Chen; C. L. Wu, A Gate-Free Monolayer Wse2 Pn Diode. *Nat Commun* **2018,** *9* (1), 3143.

[11] A. M. Jones; H. Yu; N. J. Ghimire; S. Wu; G. Aivazian; J. S. Ross; B. Zhao; J. Yan; D. G. Mandrus; D. Xiao; W. Yao; X. Xu, Optical Generation of Excitonic Valley Coherence in Monolayer Wse2. *Nature Nanotechnology* **2013,** *8* (9), 634-638.

[12] C. Zhu; D. Gao; J. Ding; D. Chao; J. Wang, Tmd-Based Highly Efficient Electrocatalysts Developed by Combined Computational and Experimental Approaches. *Chem Soc Rev* **2018,** *47* (12), 4332-4356.

[13] C. Wu; T. W. Kim; J. H. Park; H. An; J. Shao; X. Chen; Z. L. Wang, Enhanced Triboelectric Nanogenerators Based on Mos2 Monolayer Nanocomposites Acting as Electron-Acceptor Layers. *ACS Nano* **2017,** *11* (8), 8356-8363.

[14] K. Zhang; M. Peng; W. Wu; J. Guo; G. Gao; Y. Liu; J. Kou; R. Wen; Y. Lei; A. Yu; Y. Zhang; J. Zhai; Z. L. Wang, A Flexible P-Cuo/N-Mos2 Heterojunction Photodetector with Enhanced Photoresponse by the Piezo-Phototronic Effect. *Materials Horizons* **2017,** *4* (2), 274-280.

[15] P. Lin; L. Zhu; D. Li; L. Xu; C. Pan; Z. Wang, Piezo-Phototronic Effect for Enhanced Flexible Mos2/Wse2 Van Der Waals Photodiodes. *Adv Funct Mater* **2018,** *28* (35), 1802849.

[16] G. Gao; J. Yu; X. Yang; Y. Pang; J. Zhao; C. Pan; Q. Sun; Z. L. Wang, Triboiontronic Transistor of Mos2. *Adv Mater* **2019,** *31* (7), e1806905.

[17] J. Zhao; Z. Wei; Q. Zhang; H. Yu; S. Wang; X. Yang; G. Gao; S. Qin; G. Zhang; Q. Sun; Z. L. Wang, Static and Dynamic Piezopotential Modulation in Piezo-Electret Gated Mos2 Field-Effect Transistor. *ACS Nano* **2019,** *13* (1), 582-590.

[18] L. Ma; W. Hu; Q. Zhang; P. Ren; X. Zhuang; H. Zhou; J. Xu; H. Li; Z. Shan; X. Wang; L. Liao; H. Q. Xu; A. Pan, Room-Temperature near-Infrared Photodetectors Based on Single Heterojunction Nanowires. *Nano Lett* **2014,** *14* (2), 694-698.

[19] P. Guo; W. Hu; Q. Zhang; X. Zhuang; X. Zhu; H. Zhou; Z. Shan; J. Xu; A. Pan, Semiconductor Alloy Nanoribbon Lateral Heterostructures for High-Performance Photodetectors. *Adv Mater* **2014,** *26* (18), 2844-9.

[20] J. Xu; L. Ma; P. Guo; X. Zhuang; X. Zhu; W. Hu; X. Duan; A. Pan, Room-Temperature Dual-Wavelength Lasing from Single-Nanoribbon Lateral Heterostructures. *J Am Chem Soc* **2012,** *134* (30), 12394-12397.

[21] Y. Wang; W.-X. Zhou; L. Huang; C. Xia; L.-M. Tang; H.-X. Deng; Y. Li; K.-Q. Chen; J. Li; Z. Wei, Light Induced Double 'on' State Anti-Ambipolar Behavior and Self-Driven Photoswitching in P-Wse2/N-Sns2 Heterostructures. *2D Materials* **2017,** *4* (2), 025097.

[22] X. Zhang; F. Meng; J. R. Christianson; C. Arroyo-Torres; M. A. Lukowski; D. Liang; J. R. Schmidt; S. Jin, Vertical Heterostructures of Layered Metal Chalcogenides by Van Der Waals Epitaxy. *Nano Lett* **2014,** *14* (6), 3047-3054.

[23] Y.-C. Lin; R. K. Ghosh; R. Addou; N. Lu; S. M. Eichfeld; H. Zhu; M.-Y. Li; X. Peng; M. J. Kim; L.-J. Li; R. M. Wallace; S. Datta; J. A. Robinson, Atomically Thin Resonant Tunnel Diodes Built from Synthetic Van Der Waals Heterostructures. *Nature Communications* **2015,** *6* (1).

[24] Y. Gong; J. Lin; X. Wang; G. Shi; S. Lei; Z. Lin; X. Zou; G. Ye; R. Vajtai; B. I. Yakobson; H. Terrones; M. Terrones; B. K. Tay; J. Lou; S. T. Pantelides; Z. Liu; W. Zhou; P. M. Ajayan, Vertical and in-Plane Heterostructures from Ws2/Mos2 Monolayers. *Nat Mater* **2014,** *13* (12), 1135-42.

[25] B. V. Lotsch, Vertical 2d Heterostructures. *Annual Review of Materials Research* **2015,** *45* (1), 85-109.

[26] M. Y. Li; Y. Shi; C. C. Cheng; L. S. Lu; Y. C. Lin; H. L. Tang; M. L. Tsai; C. W. Chu; K. H. Wei; J. H. He; W. H. Chang; K. Suenaga; L. J. Li, Epitaxial Growth of a Monolayer Wse2-Mos2 Lateral P-N Junction with an Atomically Sharp Interface. *Science* **2015,** *349* (6247), 524-528.

[27] M.-Y. Li; J. Pu; J.-K. Huang; Y. Miyauchi; K. Matsuda; T. Takenobu; L.-J. Li, Self-Aligned and Scalable Growth of Monolayer Wse2-Mos2 Lateral Heterojunctions. *Adv Funct Mater* **2018,** *28* (17), 1706860.

[28] X. Duan; C. Wang; J. C. Shaw; R. Cheng; Y. Chen; H. Li; X. Wu; Y. Tang; Q. Zhang; A. Pan; J. Jiang; R. Yu; Y. Huang; X. Duan, Lateral Epitaxial Growth of Two-Dimensional Layered Semiconductor Heterojunctions. *Nat Nanotechnol* **2014,** *9* (12), 1024-30.

[29] C. H. Naylor; W. M. Parkin; Z. Gao; J. Berry; S. Zhou; Q. Zhang; J. B. McClimon; L. Z. Tan; C. E. Kehayias; M. Q. Zhao; R. S. Gona; R. W. Carpick; A. M.

Rappe; D. J. Srolovitz; M. Drndic; A. T. C. Johnson, Synthesis and Physical Properties of Phase-Engineered Transition Metal Dichalcogenide Monolayer Heterostructures. *ACS Nano* **2017,** *11* (9), 8619-8627.

[30] S. Xie; L. Tu; Y. Han; L. Huang; K. Kang; K. U. Lao; P. Poddar; C. Park; D. A. Muller; R. A. DiStasio, Jr.; J. Park, Coherent, Atomically Thin Transition-Metal Dichalcogenide Superlattices with Engineered Strain. *Science* **2018,** *359* (6380), 1131-1136.

[31] Y. Sun; W. M. Choi; H. Jiang; Y. Y. Huang; J. A. Rogers, Controlled Buckling of Semiconductor Nanoribbons for Stretchable Electronics. *Nat Nanotechnol* **2006,** *1* (3), 201-7.

[32] W. Wei; Y. Dai; B. Huang, Straintronics in Two-Dimensional in-Plane Heterostructures of Transition-Metal Dichalcogenides. *PCCP* **2017,** *19* (1), 663-672.

[33] Q. Sun; Y. Dai; N. Yin; L. Yu; Y. Ma; W. Wei; B. Huang, Two-Dimensional Square Transition Metal Dichalcogenides with Lateral Heterostructures. *Nano Research* **2017,** *10* (11), 3909-3919.

[34] Y. Yang; W.-H. Fang; R. Long, Disparity in Photoexcitation Dynamics between Vertical and Lateral Mos2/Wse2 Heterojunctions: Time-Domain Simulation Emphasizes the Importance of Donor–Acceptor Interaction and Band Alignment. *The Journal of Physical Chemistry Letters* **2017,** *8* (23), 5771-5778.

[35] J.-W. Jiang, Misfit Strain-Induced Buckling for Transition-Metal Dichalcogenide Lateral Heterostructures: A Molecular Dynamics Study. *Acta Mechanica Solida Sinica* **2018,** *32* (1), 17-28.

[36] A. Raja; L. Waldecker; J. Zipfel; Y. Cho; S. Brem; J. D. Ziegler; M. Kulig; T. Taniguchi; K. Watanabe; E. Malic; T. F. Heinz; T. C. Berkelbach; A. Chernikov, Dielectric Disorder in Two-Dimensional Materials. *Nat Nanotechnol* **2019,** *14* (9), 832-837.

[37] F. Barachati; A. Fieramosca; S. Hafezian; J. Gu; B. Chakraborty; D. Ballarini; L. Martinu; V. Menon; D. Sanvitto; S. Kena-Cohen, Interacting Polariton Fluids in a Monolayer of Tungsten Disulfide. *Nat Nanotechnol* **2018,** *13* (10), 906-909.

[38] J. Chen; E. Zhu; J. Liu; S. Zhang; Z. Lin; X. Duan; H. Heinz; Y. Huang; J. J. De Yoreo, Building Two-Dimensional Materials One Row at a Time: Avoiding the Nucleation Barrier. *Science* **2018,** *362* (6419), 1135-1139.

[39] Z. Zhang; P. Chen; X. Duan; K. Zang; J. Luo; X. Duan, Robust Epitaxial Growth of Two-Dimensional Heterostructures, Multiheterostructures, and Superlattices. *Science* **2017,** *357* (6353), 788-792.

[40] J. Robertson; B. Huang, Bonding and Optical Contrast in Phase Change Memory Materials. *Physica Status Solidi B-Basic Solid State Physics* **2012,** *249* (10), 1867-1873.

[41] B. Huang, Unraveling Energy Conversion Modeling in the Intrinsic Persistent Upconverted Luminescence of Solids: A Study of Native Point Defects in Antiferromagnetic Er_2o_3. *PCCP* **2016,** *18* (19), 13564-13582.

[42] B. Huang; J. Robertson, Bonding Origin of Optical Contrast in Phase-Change Memory Materials. *Physical Review B* **2010,** *81* (8).

[43] M. Sun; B. Huang, Phonon Evidence of Kohn Anomalies in Nanogenerator Zno. *Nano Energy* **2019,** *59*, 626-635.

[44] F. Ullah; Y. Sim; C. T. Le; M. J. Seong; J. I. Jang; S. H. Rhim; B. C. Tran Khac; K. H. Chung; K. Park; Y. Lee; K. Kim; H. Y. Jeong; Y. S. Kim, Growth and Simultaneous Valleys Manipulation of Two-Dimensional Mose2-Wse2 Lateral Heterostructure. *ACS Nano* **2017,** *11* (9), 8822-8829.